Spectral polarization of clear and hazy coastal skies

Raymond L. Lee, Jr.[1,*] and Orlando R. Samudio[2]

[1]Mathematics and Science Division, United States Naval Academy, Annapolis, Maryland 21402, USA

[2]1418 Spencer Avenue, New Bern, North Carolina 28560, USA

*Corresponding author: raylee@usna.edu

Received 2 July 2012; revised 14 August 2012; accepted 3 September 2012;
posted 18 September 2012 (Doc. ID 171783); published 23 October 2012

Linear polarization of the clear daytime sky has often been measured as a spectrally integrated or quasi-monochromatic variable, but seldom as a spectral one. So we use a hyperspectral imaging system to measure skylight polarization at high spectral and angular resolutions for clear and hazy skies at our coastal site. The resulting polarization maps and spectra exhibit both commonalities and differences that seem unexplained by an existing polarized radiative transfer model. Comparing the measured polarization spectra with those predicted by aerosol single scattering suggests some basic verisimilitude tests for improving such models.

OCIS codes: 010.1110, 010.1290, 010.1310, 010.7295, 290.1310, 290.5855.

1. Introduction

Polarization has been called light's "hidden variable" [1], and that reputation for stealth seems particularly apt in atmospheric optics. While even the most sophisticated optical analyses of the clear sky's brightness and color can appeal to direct visual experience, no such easy analogies exist for its polarization. Aside from Haidinger's brush (itself an intraocular phenomenon) [2–4], seeing skylight polarization has always required optical devices, even ones as simple as Brewster's pile of glass plates [5,6]. Later 19th-century polarizers and polarimeters include the Nicol prism and Savart polariscope, with the latter used to visually locate the clear sky's neutral points [7,8]. Coulson gives a short history of the polarizers and polarimeters employed to study atmospheric polarization [9].

Nowadays researchers typically measure daytime skies' polarization using dichroic linear polarizing filters mounted on digital imaging systems, with older systems relying on scanned photographic film [10–14] rather than direct digital imaging [15–19]. Skylight's linear polarization P_L is frequently measured as either a quasi-monochromatic [15,17,19–22] or spectrally integrated variable [11,12,16,23], but less often as a high-resolution spectral one [18,24,25]. To date, clear-sky P_L spectra appear to have been measured only at the zenith or in the clear-sky principal plane. Practical reasons prompt such restrictions: for example, zenith measurements of P_L eliminate its dependence on azimuth relative to the sun ϕ_{rel}. Narrow field-of-view (FOV) spectroradiometers require more time than do imaging systems to measure P_L in many different directions, so restricting P_L measurements to one plane makes good sense (see, e.g., [26,27]).

Yet such restrictions are neither necessary nor desirable now that digital imaging lets us readily analyze P_L over wide swaths of the clear sky. In particular, multispectral and hyperspectral imaging make possible measurements of the *combined* angular and spectral effects on P_L of molecular and particulate scattering. One basic problem is how to display these combined effects in a way that is both physically meaningful and easily related to everyday visual experience. Doing so will help provide useful visual and quantitative insights into how P_L spectra depend on scattering and absorption by tropospheric haze droplets and other aerosols [25,28].

Thus our scientific motivation is, in effect, to add another dimension to measurements of clear-sky polarization at visible wavelengths: the spectral

1559-128X/12/317499-10$15.00/0

dimension. This added measurement space, when combined with its corresponding angular distributions of P_L, will make possible more sophisticated verisimilitude tests of polarized atmospheric radiative transfer models. Although numerous existing studies have mapped the angular variation of clear-sky P_L [11–25], none to our knowledge have systematically mapped its spectral variation. Our work's scientific usefulness is suggested by a simple analogy: changing from monochromatic to spectral measurements of the angular distribution of unpolarized clear-sky radiances. As useful as the former are, only the latter can describe in detail the scattering-angle dependence of sky blueness, and with it the full gamut of clear-sky spectra that radiative transfer models must reproduce.

2. Measuring Skylight's Linear Polarization Spectra

A convenient and accurate way of measuring P_L with digital imaging is to use Stokes parameters I, Q, U, and V, which are irradiances that collectively determine a polarized light source's ellipsometric parameters [29]. Because skylight is mostly linearly (rather than circularly) polarized, its V is usually negligibly small [30,31]. Thus using a dichroic linear polarizer to measure

$$P_L = (Q^2 + U^2)^{1/2}/I \tag{1}$$

closely approximates the clear sky's total degree of polarization $P_T = (Q^2 + U^2 + V^2)^{1/2}/I$. In digital imaging, Stokes parameters I, Q, and U are calculated from polarized skylight radiances that illuminate each pixel on the sensor plane.

In our work, we mount a linear polarizer on the lens of a hyperspectral system, a Pika II imaging spectrometer [32] that is attached to a leveled tripod. Then we acquire in quick succession four hyperspectral datacubes of the same sky region. For each of these we manually rotate the polarizer to one of four different relative positions R so that $R = 0°$, 45°, 90°, or 135°. The $R = 0°$ position can be arbitrary so long as we do not need to know the azimuth χ of the vibration ellipse for skylight's polarized component [33,34]. Note that ellipsometric azimuths χ are different from ϕ_{rel}, the spectrometer's relative azimuth. We set $R = 0°$ when both the polarizing filter and its transmission axis are vertical.

At corresponding pixels in the $R = 0°$, 45°, 90°, and 135° datacubes, the relative spectral radiances $L_\lambda(0°)$, $L_\lambda(45°)$, $L_\lambda(90°)$, and $L_\lambda(135°)$ are related to the spectral Stokes parameters I_λ, Q_λ, and U_λ by

$$\begin{aligned} I_\lambda &= 0.5 \times [L_\lambda(0°) + L_\lambda(45°) + L_\lambda(90°) + L_\lambda(135°)], \\ Q_\lambda &= L_\lambda(0°) - L_\lambda(90°), \\ U_\lambda &= L_\lambda(45°) - L_\lambda(135°), \end{aligned} \tag{2}$$

at wavelength λ. Equation (2)'s results are used in Eq. (1) to calculate spectral linear polarization $P_{L\lambda}$. Although this simple, long-used mapping between skylight radiances and Stokes parameters [10–12,16,18] is less sophisticated than that developed by Pust and Shaw [17], our calibration analysis (see Section 3) indicates that it introduces no significant errors in measuring clear-sky $P_{L\lambda}$. For now, only minor spectral corrections to L_λ based on our calibration are required.

3. System Calibration, Performance, and Possible Error Sources

As currently configured, our Pika II spectrometer measures radiances from ~380 to 910 nm with a spectral resolution of ~4.5 nm and has an analog–digital brightness resolution of 12 bits for each of its 120 spectral channels. Its 8 mm Schneider lens has a nominal FOV ~33.4°, and each hyperspectral pixel subtends a linear angle of ~0.045°. Scan rates are always a compromise between speed of data acquisition and quantized radiometric noise in those data. For the Pika II, a speed of 64 lines/s gives a good balance between speed and noise, generating a 640-by-1000 pixel datacube in ~16 s. However, the time required for (1) the rotation stage's return slew and backlash correction and (2) rotating the polarizer increases this interval to ~33 s per datacube [32]. Pixel registration errors measured among $P_{L\lambda}$ datacubes usually are <1 pixel (<1:640 per line), and these stem from small positioning errors by the rotation stage between scans.

System manufacturer Resonon, Inc. provided an absolute radiometric calibration for the Pika II. Each of the 640 pixels that make one scanline has its own spectral calibration, and the calibration procedure follows National Institute of Standards and Technology recommendations. Resonon's calibration did not include the B + W Kaesemann-type polarizing filter we use, but two salient points here are that (1) the filter's measured spectral transmittance T_λ is nearly uniform for unpolarized visible light (mean $T_\lambda = 0.3206$), and (2) more importantly, T_λ varies negligibly with R for a given pixel. In other words, Kaesemann polarizers by design have highly spatially uniform T_λ, so rotating them has a minimal effect on measured $P_{L\lambda}$.

A polarizer's optical performance is partly specified by its extinction coefficient H_{90}, the combined transmittance of initially unpolarized light by two such polarizers whose transmission axes are perpendicular. As measured with a separate narrow-FOV spectroradiometer [35], our polarizer has an average visible wavelength $H_{90} = 0.001127$, and its major and minor principal transmittances k_1 and k_2 are 0.6394 and 0.001763, respectively. Although the polarizer's H_{90} is fairly uniform at visible wavelengths, a crossed pair of such polarizers do transmit a dim violet when lit by a white light source. This fairly common "blue leak" corresponds to a maximum spectral transmissivity = 0.008727 at 400 nm; the intrinsic filter polarization = 0.9945 for incident unpolarized light. Given that the clear sky's maximum

$P_L \sim 0.85$, this polarizer is more than adequate for our work.

Because we rotate the polarizer manually, slight alignment errors of the filter are inevitable. Based on our measurements, these rotational errors are at most ~2°–3° from the marks ruled at 45° intervals on the polarizer's edge. If we put the k_1 and k_2 values given above into the Mueller matrix for a linear polarizer [36] and then simulate the polarization errors that result from 20,000 such random misalignments, the mean reduction in P_L is <0.5% compared with its true value (e.g., $P_L = 0.7$ would be reduced to $P_L \sim 0.697$). Both the alignment errors and blue leak slightly depolarize the measured $P_{L\lambda}$ spectra. Other sources of P_L errors can be more significant, as noted below.

Depending on one's priorities, these significant errors may not include slight misaiming of the spectrometer in ϕ_{rel} and view-elevation angle h ($h = 0°$ at the astronomical horizon and 90° at the zenith). We use sun shadows cast by a gnomon on the Pika II to estimate ϕ_{rel} to within ~3° and a digital inclinometer placed on it to measure h accurate to within ~0.1°–0.2°. Furthermore, during the ~100 s that elapses between the $R = 0°$ and $R = 135°$ scans, changes in the sun's unrefracted elevation h_0 and azimuth typically change both ϕ_{rel} and h_0 by ~0.3°. For astronomical work, these combined uncertainties would be unacceptably large. However, because our initial goals are to measure $P_{L\lambda}$ spectra *throughout* a sky region and to make *qualitative* comparisons with modeled $P_{L\lambda}$ spectra, such aiming uncertainties are acceptable for now. In particular, the ϕ_{rel} uncertainty is tolerable because P_L changes fairly slowly with azimuth.

A subtler problem for imaging polarimeters is self-polarization caused by lens refraction [37–39]. For rays entering a lens surface at nonnormal incidence, the camera optical train itself slightly polarizes the transmitted light, and the amount of this self-polarization increases with incidence angle. If a linear polarizer precedes the lens, the lens then acts as a weak analyzer. As a result, the combination reduces transmitted L by an amount that depends on filter orientation, even for unpolarized incident light. Gerharz's analysis indicates that a typical lens's maximum self-polarization is ~0.10 [37,40].

Our measurements of an unpolarized light source (a diffusely reflected incandescent projector beam) yield similar results. In the Pika II, self-polarization is wavelength-dependent and if uncorrected can increase spectrally integrated P_L by ~0.05 and $P_{L\lambda}$ even more than that at ~400 nm. Working from hyperspectral data for this unpolarized light source, a preliminary solution is to define software spectral filters for the four different $L_\lambda(R)$. With these corrections to unpolarized Pika II data, the residual self-polarization has a mean $P_{L\lambda} = 0.00415$ at visible wavelengths (396.774–701.958 nm) and a 95th-percentile $P_{L\lambda} < 0.014$, a significant improvement over the uncorrected mean $P_{L\lambda} = 0.0642$.

Table 1 presents summary statistics that describe the Pika II's polarization performance. To calculate Table 1, we use the Pika II and Eqs. (1) and (2) to measure $P_{L\lambda}$ produced by the B + W Kaesemann polarizer itself (this requires a pair of such polarizers). We then compare this Pika II spectrum with the filter's known intrinsic spectral polarization $P_{L\lambda,i}$ [35]. At visible wavelengths, $P_{L\lambda,i} \sim 1$, and the difference $\Delta P_{L\lambda} = P_{L\lambda} - P_{L\lambda,i}$ is positive when the Pika II overestimates $P_{L\lambda,i}$ and is negative when it underestimates $P_{L\lambda,i}$ (note that $P_{L\lambda}$ never exceeds 1). Table 1's first row is the mean value of $\Delta P_{L\lambda}$ for the indicated spectral interval, and its second row is the corresponding standard deviation s. Table 1's third row is the mean signal-to-noise ratio SNR($P_{L\lambda}$), which is calculated as the ratio of the mean Pika II $P_{L\lambda}$ to its standard deviation on the given spectral interval. Note that this ratio is a measure of noise in $P_{L\lambda}$ rather than in $\Delta P_{L\lambda}$ and so cannot be calculated from Table 1's first two rows. Although SNR ($P_{L\lambda}$) clearly is smallest at short wavelengths, even there its value greatly exceeds the minimum Rose criterion of 5:1. Thus these statistics collectively demonstrate that the Pika II system can calculate $P_{L\lambda}$ accurately at visible wavelengths, the interval of interest here.

4. Measured Polarization Spectra in Clear and Hazy Skies

From 2009 to 2012, one of us (R. Lee) measured polarization spectra for over 30 clear to partly cloudy skies at two coastal sites: Bar Harbor, Maine, and the United States Naval Academy (USNA) in Annapolis, Maryland. Here we analyze the more numerous USNA clear-sky measurements of spectral $P_{L\lambda}$ and spectrally integrated P_L. Figures 1(a) and 1(b) show visible-wavelength maps of $P_{L\lambda}$ and P_L, respectively, measured with the Pika II on the afternoon of 20 September 2010; each map's angular dimensions are ~29° by 46.5°. During scanning for Fig. 1, the mean $h_0 = 30.8°$ and $\phi_{\text{rel}} \sim 90°$ at image center. Note that ϕ_{rel} increases from 0° at the sun's azimuth as an observer looks clockwise around the horizon (seen near each map's base), and so the sun is to the left of Figs. 1(a) and 1(b).

We created Fig. 1(a)'s false-color map by treating its underlying invisible $P_{L\lambda}$ spectra as if they were spectral power distributions of visible light sources.

Table 1. Calibration Summary Statistics for Pika II Imaging Spectrometer

Wavelength interval (nm)	400–450	450–500	500–550	550–600	600–650	650–700
Mean $\Delta P_{L\lambda}$	–0.01143	0.002903	0.0007798	–0.002869	–0.007816	–0.01481
s (mean $\Delta P_{L\lambda}$)	0.04391	0.001419	0.0005202	0.001571	0.001539	0.001689
Mean SNR ($P_{L\lambda}$)	17.95:1	295.7:1	2178:1	638.2:1	645.1:1	578.6:1

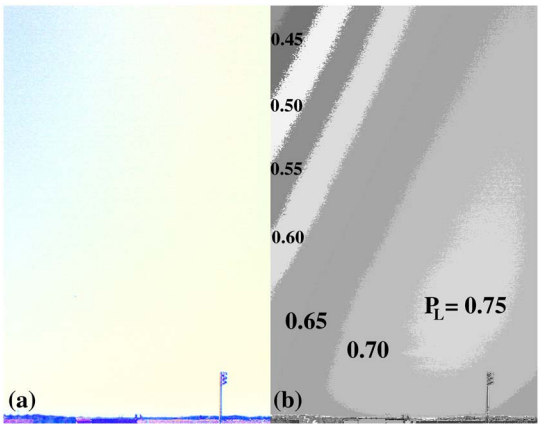

Fig. 1. (Color online) Linear polarization measured at visible wavelengths $\lambda = 400$–700 nm in a clear, haze-free sky at the United States Naval Academy (USNA) in Annapolis, Maryland, on the afternoon of 20 September 2010. Hyperspectral data are shown as either (a) a false-color map of spectral polarization $P_{L\lambda}$ or (b) a binned gray-scale map of spectrally integrated degree of polarization P_L. Unrefracted sun elevation $h_0 = 30.8°$ and azimuth relative to the sun $\phi_{\text{rel}} \sim 90°$ at each map's center.

For each of these 400–700 nm $P_{L\lambda}$ spectra, we calculate (1) the corresponding 1931 CIE x, y chromaticities [41] and (2) their red-green-blue (RGB) equivalents on a computer's calibrated color display [42]. Then we use these RGB equivalents to generate Fig. 1(a)'s colors, each of which is plotted at maximum brightness. Thus Fig. 1(a) only gives information on each pixel's *spectral* distribution of $P_{L\lambda}$, not on its magnitude. Naturally, other false-color mappings than ours are possible, but ours does solve the problem posed in Section 1: how to relate skylight's spectral polarization to everyday visual experience. In other words, Fig. 1(a) suggests what the clear sky would look like if we could actually detect $P_{L\lambda}$ spectra. To make differences among these polarization colors easier to see, we apply a uniform color-contrast enhancement to all such maps.

What optical information does Fig. 1(a)'s color provide? First, note that its nearly uniform yellow near $h = 0°$ becomes slightly bluish at larger h on its left side where $\phi_{\text{rel}} < 90°$. Although this change is subtle, it clearly indicates that systematic angular changes in $P_{L\lambda}$ can occur in a given clear sky. For some meteorological context, Table 2 lists data on surface humidity and sky state for 20 September 2010, as well as normal aerosol optical depths $\tau_{\text{aer},\lambda}$ measured at a nearby sun photometer site [43]. In fact, this haze-free day had among the smallest $\tau_{\text{aer},\lambda}$ and best visibility conditions of those measured.

Figure 1(b)'s gray-scale map results from binning spectrally integrated P_L into bands of width 0.05 (e.g., the band labeled "0.60" spans $0.60 \le P_L < 0.65$). Along Fig. 1(b)'s vertical midline, the single-scattering angle Ψ between the sun and viewing direction decreases from $\Psi \sim 90°$ at the visible horizon (which is slightly above $h = 0°$) to $\Psi \sim 68°$ at the map's top. In a single-scattering molecular atmosphere, the maximum clear-sky P_L occurs along the great circle where $\Psi = 90°$, including this circle's intersection with the astronomical horizon.

Yet in Fig. 1(b), the maximum P_L occurs above the horizon and at $\phi_{\text{rel}} > 90°$, a shift largely caused by large increases in slant-path optical thickness τ_{slant} near $h = 0°$ [12]. As τ_{slant} increases, so do multiple scattering and its associated depolarization, with the net result that P_L maxima are displaced upward from the horizon. Corollary evidence in Fig. 1(b) for this strong depolarization is the distinct flattening and widening of the $P_L = 0.70$ band just above the horizon. To a much lesser extent, scattering by aerosols also shifts the peak P_L to larger Ψ and ϕ_{rel} in Fig. 1(b). Finally, note that the P_L bands' long axes are tilted ~30° from the vertical or roughly parallel to $\Psi = 90°$, as one would expect for $h_0 \sim 30°$.

Figure 2 maps polarization in the antisolar sky ~10 min earlier on 20 September 2010 (see Table 2 for details). Figure 2(b) has some familiar features: (1) at $\phi_{\text{rel}} = 180°$, the map's P_L values steadily decrease toward the horizon (and toward the subhorizon Arago neutral point [8]), and (2) the map's individual P_L bands widen slightly near the horizon, just as in Fig. 1(b). Less familiar is Fig. 2(a)'s orangish sky, the result of a distinct spectral shift in $P_{L\lambda}$. Figure 3's plot of visible-wavelength $P_{L\lambda}$ spectra for Figs. 1 and 2 quantifies this shift: at $\phi_{\text{rel}} = 180°$, $P_{L\lambda}$ steadily increases for $\lambda > 430$–440 nm except for a broad local maximum near 650 nm [44]. This trend produces Fig. 2(a)'s orangish antisolar sky. By contrast, neither of Fig. 3's two $P_{L\lambda}$ spectra at $\phi_{\text{rel}} = 90°$ exhibit any consistent trend at longer wavelengths, with the net result that Fig. 1(a)'s map is only slightly yellowish. Spectra for $\phi_{\text{rel}} = 90°$ closely resemble those of polarization maxima that Coulson measured, although his data appear to be from the principal plane (i.e., at $\phi_{\text{rel}} = 180°$) [22]. In Fig. 3 and later figures, $P_{L\lambda}$ is shown at $h = 5°$ and 10° because the consequences of multiple scattering are most pronounced over these long optical paths. Note that Fig. 3's narrow minima and maxima for $\lambda < 430$ nm negligibly affect their corresponding color maps [Figs. 1(a) and 2(a), respectively]. We

Table 2. Meteorological Conditions and Aerosol Normal Optical Depths

Figure(s)	Date	h_0 Interval (°)[a]	Surface T (°C)	Surface RH (%)	Clear-Sky State	$\tau_{\text{aer},380\text{ nm}}$	$\tau_{\text{aer},440\text{ nm}}$	$\tau_{\text{aer},500\text{ nm}}$	$\tau_{\text{aer},675\text{ nm}}$
1 and 2	20-9-2010	30.8–32.9	23.6	24.9	No haze	0.05346	0.04430	0.03720	0.02481
4 and 5	13-9-2011	32.9–29.1	28.9	57.6	Haze	0.3568	0.2799	0.2266	0.1200
7(a) and 7(b)	13-4-2012	33.3–39.6	18.1	29.1	No haze	0.1618	0.1367	0.1203	0.08270

[a]For a given date, h_0 values are listed in figure-number order. Our observing site is at the United States Naval Academy in Annapolis, Maryland (38° 59′ N, 76° 29′ W, elevation ~20 m).

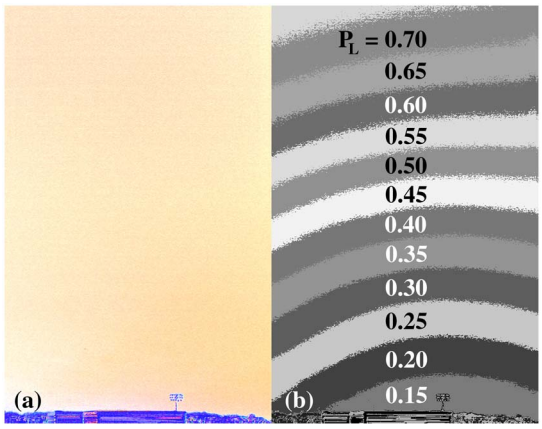

Fig. 2. (Color online) Maps of (a) $P_{L\lambda}$ and (b) P_L as in Fig. 1, but for $h_0 = 32.9°$, $\phi_{rel} \sim 180°$ at USNA on 20 September 2010.

examine Fig. 3's implications for polarization theory in Section 5.

For the hazy day of 13 September 2011, Fig. 4 shows pronounced changes in both integrated P_L and $P_{L\lambda}$ spectra. Table 2 indicates that the $\tau_{aer,\lambda}$ are much larger on this date, with corresponding increases in multiple scattering at all wavelengths. As a result, in Fig. 4(b) the maximum polarization at $\phi_{rel} = 270°$ [45] decreases to $P_L < 0.50$, while the angular width of each P_L band increases as the map's total range of P_L decreases. Figure 4(a) shows the spectral consequences of increased aerosol scattering, with colorimetrically purer oranges replacing Fig. 1(a)'s desaturated yellows. Also note in Fig. 4(a) that the purity of polarization colors increases at small h even as P_L itself decreases.

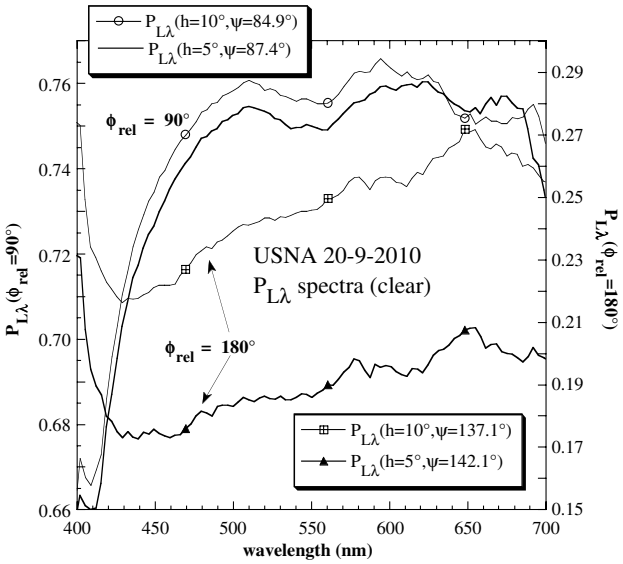

Fig. 3. Mean $P_{L\lambda}$ spectra for view-elevation angles $h = 5°$ and 10° calculated from hyperspectral data for Figs. 1 and 2 (haze-free sky of 20 September 2010). Averages are for an area of angular size $\Delta h = 2°$, $\Delta\phi_{rel} = 4°$ that is centered on the indicated ϕ_{rel} and h. Each spectrum is also labeled with its corresponding single-scattering angle Ψ; note that ordinate scales differ for the two values of ϕ_{rel}.

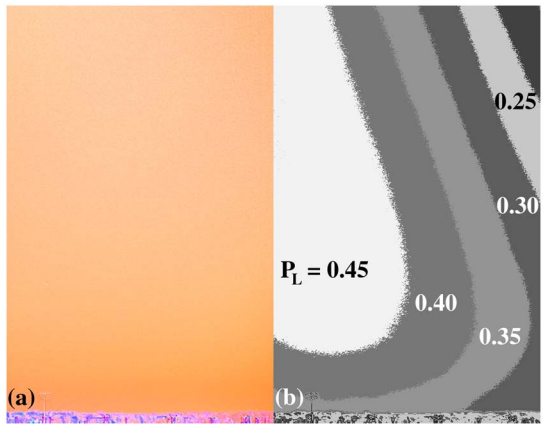

Fig. 4. (Color online) Maps of (a) $P_{L\lambda}$ and (b) P_L as in Fig. 1, but for $h_0 = 32.9°$, $\phi_{rel} \sim 270°$ at USNA on the hazy morning of 13 September 2011.

For the antisolar sky of 13 September 2011, Fig. 5 shows similar (1) spectral shifts in $P_{L\lambda}$ and (2) decreases in both P_L and its range. Not only are the $P_{L\lambda}$ spectra at $\phi_{rel} = 180°$ distinctly more orange in Fig. 5(a) than in Fig. 2(a), but they are purplish for small h where $P_L < 0.10$ [see Fig. 5(b)]. Figure 6 illustrates how these two trends in P_L and $P_{L\lambda}$ are paired. As h increases in Fig. 4 ($\phi_{rel} = 270°$), its $P_{L\lambda}$ spectra increase in magnitude even as their upward slopes decrease, and thus Fig. 4(a)'s oranges become less saturated. However, increasing h in Fig. 5 ($\phi_{rel} = 180°$) at first causes both the magnitudes *and* slopes of $P_{L\lambda}$ spectra to increase, with the result that colors in Fig. 5(a) shift from purplish to orange. Above $h \sim 15°$ in Figs. 4 and 5, the shapes of the $P_{L\lambda}$ spectra shift very little as their magnitudes steadily increase.

5. Plausible Explanations, Some Pitfalls, and the State of Modeling

A reasonable explanation for these paired $P_{L\lambda}$ trends in the hazy sky of Figs. 4 and 5 is that as aerosol scattering and absorption grow, increased multiple scattering somehow makes these processes' spectral

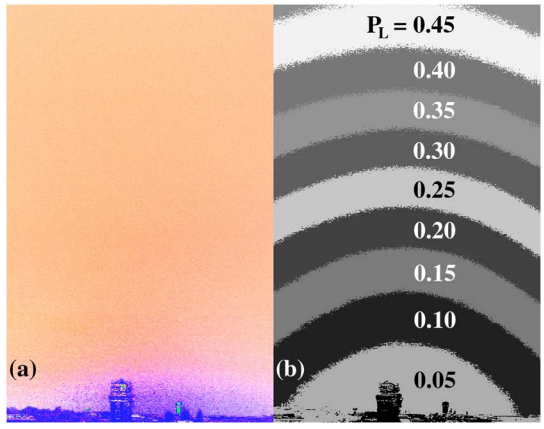

Fig. 5. (Color online) Maps of (a) $P_{L\lambda}$ and (b) P_L as in Fig. 4, but for $h_0 = 29.1°$, $\phi_{rel} \sim 180°$ at USNA on 13 September 2011.

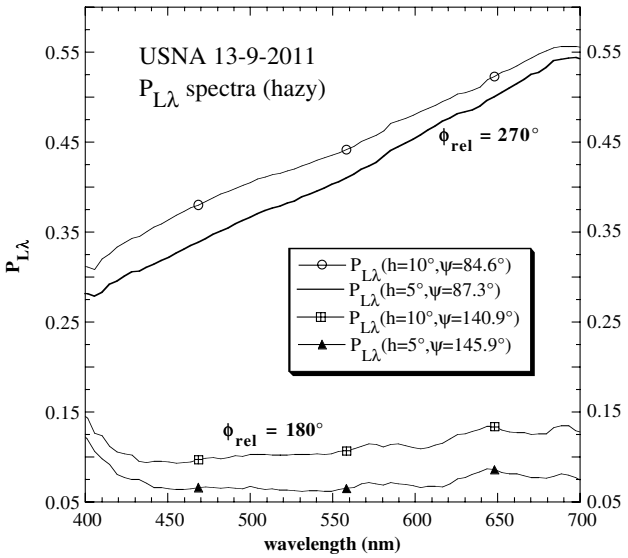

Fig. 6. Mean $P_{L\lambda}$ spectra as in Fig. 3, but calculated from hyperspectral data for Figs. 4 and 5 (hazy sky of 13 September 2011) and having a single ordinate scale.

stamps stronger, especially near the horizon where τ_{slant} increases quickly with decreasing h. As mean $\tau_{\text{aer},\lambda}$ increases along these slant paths, Figs. 2–6 all indicate that the spectrum of $P_{L\lambda}$ is shifted toward longer wavelengths, with the resulting oranges being purest near the horizon. While similar arguments can be made for $P_{L\lambda}$ spectra due to molecular scattering, these spectra are nearly constant with wavelength [31,46] and so seem unlikely to affect polarization color.

However, Fig. 7 complicates this tidy picture. It juxtaposes the $P_{L\lambda}$ color maps in Figs. 7(a) and 7(b) ($\phi_{\text{rel}} = 90°$ and 180°, respectively) for 13 April 2012, a day with no visible haze and intermediate $\tau_{\text{aer},\lambda}$ values (see Table 2). One problem is that Fig. 7(b)'s antisolar $P_{L\lambda}$ color gamut is *not* intermediate to those of Figs. 2(a) and 5(a), even though these bracket Fig. 7(b)'s aerosol optical depths. Instead, Fig. 7(b) is dominated by yellows and oranges that

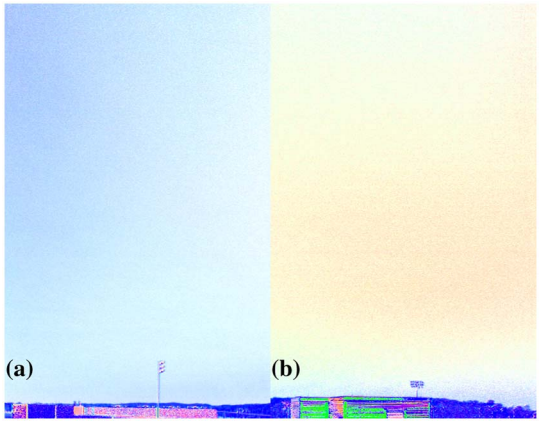

Fig. 7. (Color online) False-color maps of $P_{L\lambda}$ at (a) $h_0 = 33.3°$, $\phi_{\text{rel}} \sim 90°$ and (b) $h_0 = 39.6°$, $\phi_{\text{rel}} \sim 180°$ at USNA on the clear, apparently haze-free afternoon of 13 April 2012.

are less saturated than the oranges found in either Fig. 2(a) or 5(a). Similarly, the bluish $P_{L\lambda}$ spectra seen in Fig. 7(a) cannot easily be inferred from the yellows and oranges in Figs. 1(a) and 4(a), although some blues do appear at smaller ϕ_{rel} in Fig. 1(a).

So predicting the angular distribution of $P_{L\lambda}$ spectra apparently requires more than simply knowing a site's total optical depth τ_{aer} or even its $\tau_{\text{aer},\lambda}$. The latter point is made by Fig. 8, in which Table 2's $\tau_{\text{aer},\lambda}$ spectra are plotted. If these spectra are normalized to have a common maximum, their shapes (and thus Angström coefficients) are nearly identical, which implies that measurements of aerosol spectral extinction may not be sufficient to explain the full gamut of $P_{L\lambda}$ spectra. Two other variables to scrutinize are the species inventory and vertical distribution of local aerosols [47,48], although we currently lack such data.

Yet even with no constraints on aerosol data, satisfactorily explaining the polarization spectra seen in Figs. 1–7 requires a model able to incorporate these data. Unlike the plethora of unpolarized radiative transfer models, relatively few full-featured models of atmospheric polarization are available for testing [46,49–51]. The polarized model developed by Evans and Stephens uses the doubling and adding method in a plane-parallel atmosphere to calculate Stokes parameters I, Q, U, and V in any direction for the desired number of radiation streams [50]. This polRadTran model can be downloaded from the libRadtran site [52] as one of several radiative-transfer algorithms that incorporate detailed data on the thermal, molecular, and aerosol properties of simulated atmospheres.

In Figs. 9 and 10 we simulate $P_{L\lambda}$ using polRadTran and a "clean maritime" aerosol mixture appropriate for our site from the OPAC model [53]. We multiply OPAC aerosol concentrations by a constant

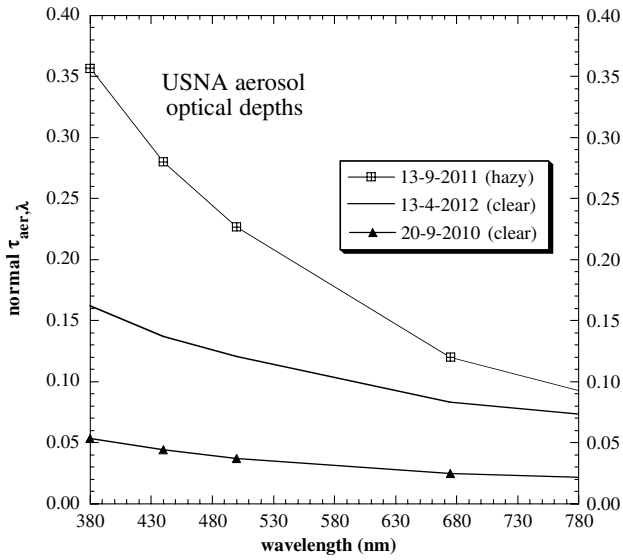

Fig. 8. Aerosol normal optical depths $\tau_{\text{aer},\lambda}$ measured at AERONET sun photometer sites near USNA at the times closest to those of Figs. 1–7.

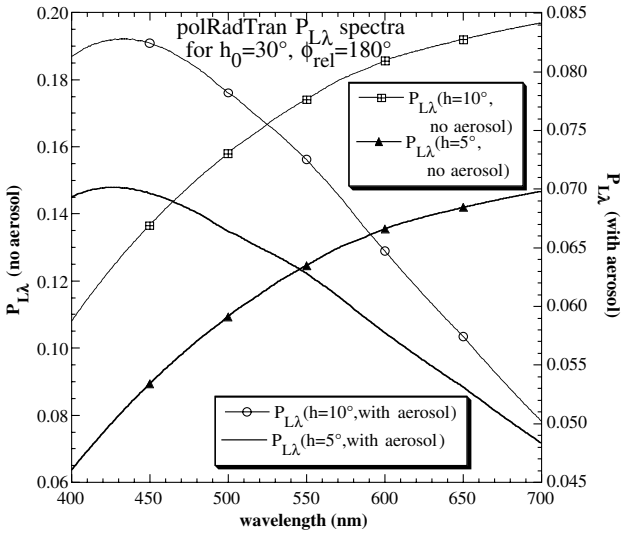

Fig. 9. Spectral polarization $P_{L\lambda}$ for $h_0 = 30°$, $h = 5°$ and 10° at $\phi_{rel} = 180°$ as calculated by the polRadTran model for atmospheres either without aerosols or with $\tau_{aer,\lambda}$ approximating that measured at USNA on 13 September 2011 (hazy sky). The Lambertian surface reflectance = 0.2 at all wavelengths.

so that polRadTran's calculated $\tau_{aer,\lambda}$ at 440 nm closely matches that measured for Figs. 4–6 (the hazy sky of 13 September 2011; see Table 2). Initial polRadTran results are somewhat puzzling. For a model atmosphere without aerosols, its antisolar $P_{L\lambda}$ in Fig. 9 increase monotonically with λ and their spectra steepen as the elevation angle increases from $h = 5°$ to 10° [54]. Minus spectral details, these are essentially the spectral trends measured in Fig. 6 at $\phi_{rel} = 180°$. However, if aerosols are added to polRadTran's atmosphere, then Fig. 9's $P_{L\lambda}$ spectra *decrease* monotonically for $\lambda > 430$ nm at $\phi_{rel} = 180°$ (see Fig. 10), unlike both a purely molecular atmosphere and our measured haze-free one (Figs. 2 and 3).

At $\phi_{rel} = 90°$ (Fig. 11), the polRadTran results are rather a mixed lot. For example, polRadTran's hazy atmosphere in Fig. 11 once again has bluish, not orangish, $P_{L\lambda}$ spectra. This model trend is just the opposite of that in the corresponding measured spectra (see Figs. 6 and 12). Only by removing aerosols completely can we generate orange spectra in Fig. 11 that resemble those in the hazy skies of Figs. 4 and 6. Yet polRadTran's bluish $P_{L\lambda}$ spectra *are* qualitatively

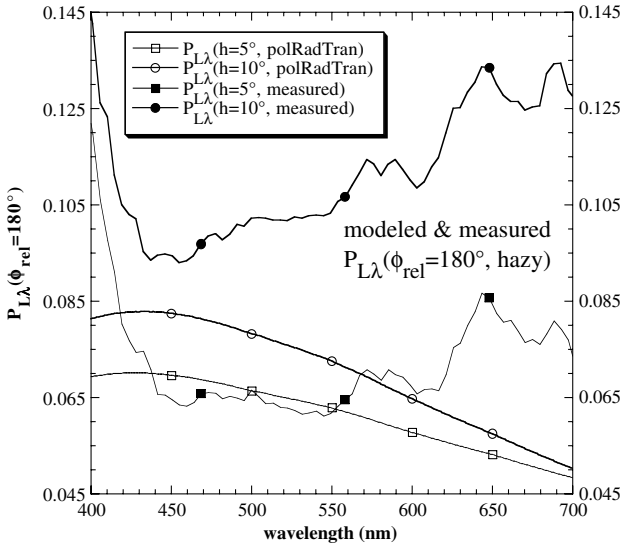

Fig. 10. Comparison of polRadTran simulated $P_{L\lambda}$ spectra for Fig. 9's $\phi_{rel} = 180°$ aerosol case (representative of our site's aerosols) and corresponding measured $P_{L\lambda}$ spectra from Fig. 6. Spectra for $h = 5°$ are marked with open or solid squares, whereas $h = 10°$ spectra are marked with open or solid circles.

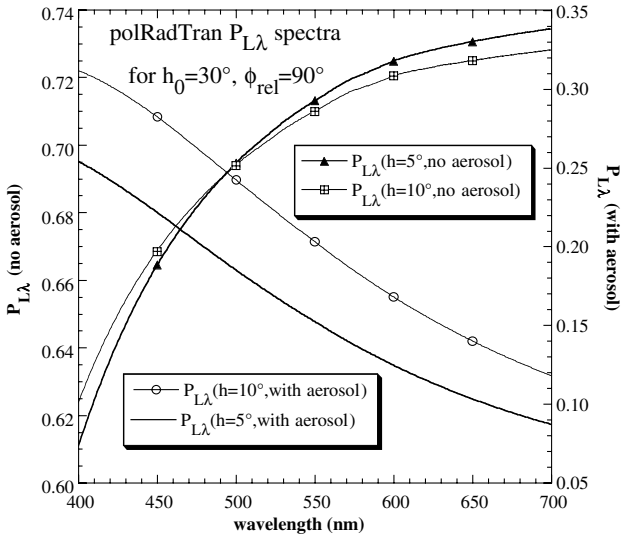

Fig. 11. Same as Fig. 9, but for $\phi_{rel} = 90°$ in polRadTran.

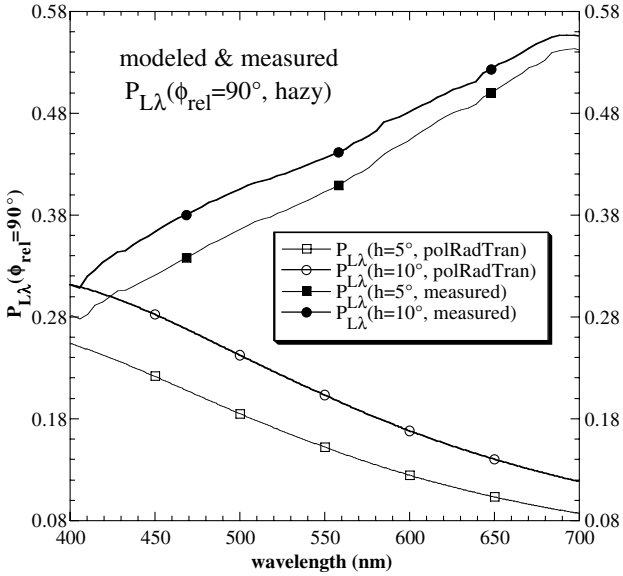

Fig. 12. Comparison of polRadTran simulated $P_{L\lambda}$ spectra for Fig. 11's $\phi_{rel} = 90°$ aerosol case (representative of our site's aerosols) and corresponding measured $P_{L\lambda}$ spectra from Fig. 6, where $\phi_{rel} = 270°$. Spectra for $h = 5°$ are marked with open or solid squares, whereas $h = 10°$ spectra are marked with open or solid circles.

consistent with those from Fig. 7(a), and the model's spectra at $\phi_{rel} = 90°$ do not change shape even if we reduce its $\tau_{aer,\lambda}$ to match Fig. 7 (see Table 2). In short, polRadTran's errors are not fixed just by adjusting its aerosols: no realistic combinations of OPAC aerosol parameters could match all of our measured $P_{L\lambda}$ spectra.

Our point here is not to raise unfairly high bars for polRadTran to clear. Instead, we merely want to approximate our measured spectral and angular $P_{L\lambda}$ trends, a standard that any model must meet. At least based on our measurements, although polRadTran provides a reasonable first step toward that goal, other models must also be evaluated. Among these are a polarized successive orders of scattering model [28,51], the MYSTIC polarized Monte Carlo model [46], and a forthcoming polarized version of MODTRAN [48].

Figure 13 suggests one basic verisimilitude test for these models. It plots spectral polarization by single scattering from absorbing aerosols at $\Psi = 145°$ (equivalent to $h = 5°$, $\phi_{rel} = 180°$ for $h_0 = 30°$) and at $\Psi = 87.5°$ ($h = 5°$, $\phi_{rel} = 90°$ for $h_0 = 30°$); see Fig. 3 for comparison. In Fig. 13 we invoke aerosols that have either wavelength-independent optical constants $n = 1.5$ and $k = 0.01$ [55] or a somewhat more detailed n, k wavelength dependence for a mixture of aerosol species typical of our region [47,56]. Then for each n, k type, we weight a droplet's scattered Stokes parameters [31] by the number density for its radius in Deirmendjian's haze-M size distribution [55].

The resulting $P_{L\lambda}$ spectra suggest some fundamental criteria for modeling: (1) depending on the haze-M distribution's maximum droplet radius, Fig. 13's $P_{L\lambda}$ spectra can be made bluish near the antisolar horizon ($\Psi = 145°$ curves), with orangish $P_{L\lambda}$ spectra (not shown) at larger h, and (2) for all species and h at $\phi_{rel} = 90°$ or 270°, aerosol $P_{L\lambda}$ spectra are orangish to varying degrees. Behavior (1) resembles the measured h dependence of $P_{L\lambda}$ above the antisolar horizon (see Figs. 5 and 6), while behavior (2) is evident in Figs. 1 and 4 at $\phi_{rel} = 90°$ and 270°. Note that $P_{L\lambda}$ differs little between constant n, k and the more complicated three-species mixture, indicating that for coastal haze conditions typical of our region, aerosol sizes matter more than their composition [57]. Although such simple exercises omit scattering by molecules and multiple scattering, they may well be useful in vetting the polarization behavior of more sophisticated models that do include these processes.

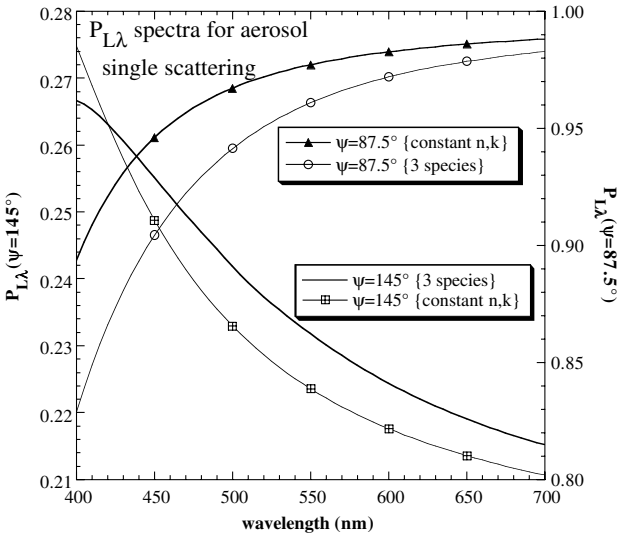

Fig. 13. Spectral polarization $P_{L\lambda}$ at indicated Ψ for single scattering by a haze-M polydispersion with droplet radii ≤0.1 μm. Complex refractive indices n and k for these aerosols either (a) are spectrally constant at $n = 1.5$, $k = 0.01$ or (b) have the weak spectral dependence of a three-species aerosol mixture typical of our region. Note that ordinate scales differ for the two Ψ.

6. Conclusions

Our work here is necessarily a preliminary report on how clear-sky polarization spectra depend on scattering angle, sun elevation, and aerosol type and concentration. We have yet to assess how large variations in surface spectral reflectances affect $P_{L\lambda}$ spectra [58], although our coastal location is well suited to this task. Adding inland measurement sites and their different aerosol types certainly would yield instructive new variations on our existing $P_{L\lambda}$ datasets. We also plan to refine the Pika II imager's calibration to account in greater detail for self-polarization and other imager-related polarization artifacts [59].

Nonetheless, we have filled in some considerable blanks in our existing knowledge. First, we now know that orangish $P_{L\lambda}$ spectra are the norm at $\phi_{rel} \sim 90°$ or 270° and that the slopes of these spectra *tend* to increase with aerosol optical depth. Second, the magnitude and shape of $P_{L\lambda}$ spectra appear to be only partly dependent on $\tau_{aer,\lambda}$, with other likely candidates being the vertical distribution and (perhaps) mixture of aerosol species. Third, despite the potential of models such as polRadTran, our literature review and model testing suggest that truly robust, realistic simulations of $P_{L\lambda}$ spectra have yet to be identified. The additional modeling constraints provided by measured polarization spectra follow from our original scientific motivation and, we believe, clearly demonstrate the scientific utility of our work. Thus as we had originally intended, the descriptive and prescriptive power of hyperspectral imaging has helped make spectral polarization of clear and hazy skies much less a "hidden" variable and more a visible, utilitarian one.

R. L. Lee was generously supported by United States National Science Foundation grants AGS-0914535 and AGS-0540896 and by the United States Naval Academy's Departments of Oceanography and Physics. Opinions, findings, and conclusions or recommendations expressed in this paper are those of the authors and do not necessarily reflect the views of the National Science Foundation.

References and Notes

1. C. F. Bohren and E. E. Clothiaux, *Fundamentals of Atmospheric Radiation* (Wiley-VCH, 2006), p. 345.
2. G. Können, *Polarized Light in Nature* (Cambridge, 1985), pp. 11–12.
3. D. Pye, *Polarised Light in Science and Nature* (Institute of Physics, 2001), pp. 117–118.
4. A. Le Floch, G. Ropars, J. Enoch, and V. Lakshminarayanan, "The polarization sense in human vision," Vis. Res. **50**, 2048–2054 (2010).
5. D. Brewster, "On the polarisation of light by oblique transmission through all bodies, whether crystallized or uncrystallized," Philos. Trans. R. Soc. Lond. **104**, 219–230 (1814).
6. D. Brewster, "On the polarization of the atmosphere," Philos. Mag. **31**, 444–454 (1847).
7. M. Richartz, "An improvement of Savart's polariscope," J. Opt. Soc. Am. **38**, 623–625 (1948).
8. H. Neuberger, *Introduction to Physical Meteorology* (Pennsylvania State University, 1957), pp. 196–199.
9. K. L. Coulson, *Polarization and Intensity of Light in the Atmosphere* (A. Deepak, 1988), pp. 533–546, 551–567.
10. R. Walraven, "Polarization imagery," Opt. Eng. **20**, 14–18 (1981).
11. J. A. North and M. J. Duggin, "Stokes vector imaging of the polarized sky-dome," Appl. Opt. **36**, 723–730 (1997).
12. R. L. Lee, Jr., "Digital imaging of clear-sky polarization," Appl. Opt. **37**, 1465–1476 (1998).
13. J. Gál, G. Horváth, V. B. Meyer-Rochow, and R. Wehner, "Polarization patterns of the summer sky and its neutral points measured by full-sky imaging polarimetry in Finnish Lapland north of the Arctic Circle," Proc. R. Soc. Lond. A **457**, 1385–1399 (2001).
14. B. Suhai and G. Horváth, "How well does the Rayleigh model describe the *E*-vector distribution of skylight in clear and cloudy conditions? a full-sky polarimetric study," J. Opt. Soc. Am. A **21**, 1669–1676 (2004).
15. Y. Liu and K. J. Voss, "Polarized radiance distribution measurement of skylight. II. Experiment and data," Appl. Opt. **36**, 8753–8764 (1997).
16. M. V. Berry, M. R. Dennis, and R. L. Lee, Jr., "Polarization singularities in the clear sky," New J. Phys. **6**, 162 (2004).
17. N. J. Pust and J. A. Shaw, "Dual-field imaging polarimeter using liquid crystal variable retarders," Appl. Opt. **45**, 5470–5478 (2006).
18. T. W. Cronin, E. J. Warrant, and B. Greiner, "Celestial polarization patterns during twilight," Appl. Opt. **45**, 5582–5589 (2006).
19. N. J. Pust and J. A. Shaw, "Digital all-sky polarization imaging of partly cloudy skies," Appl. Opt. **47**, H190–H198 (2008).
20. T. Gehrels, "Wavelength dependence of the polarization of the sunlit sky," J. Opt. Soc. Am. **52**, 1164–1173 (1962).
21. D. J. Gambling and B. Billard, "A study of the polarization of skylight," Aust. J. Phys. **20**, 675–681 (1967).
22. K. L. Coulson, *Polarization and Intensity of Light in the Atmosphere* (A. Deepak, 1988), pp. 284–286, 291, 300, 305–307, 418, 421–422. Coulson's visible-wavelength P_L measured at Mauna Loa, Hawaii, have a fairly coarse spectral resolution of 100 nm.
23. C. Bellver, "Luminance and polarization of the sky light at Seville (Spain) measured in white light," Atmos. Environ. **22**, 595–599 (1988).
24. I. Aben, F. Helderman, D. M. Stam, and P. Stammes, "Spectral fine-structure in the polarisation of skylight," Geophys. Res. Lett. **26**, 591–594 (1999).
25. E. Boesche, P. Stammes, T. Ruhtz, R. Preusker, and J. Fischer, "Effect of aerosol microphysical properties on polarization of skylight: sensitivity study and measurements," Appl. Opt. **45**, 8790–8805 (2006).
26. K. L. Coulson, "Effects of the El Chichon volcanic cloud in the stratosphere on the polarization of light from the sky," Appl. Opt. **22**, 1036–1050 (1983).
27. C. Bellver, "Study of luminance and polarimetry of the sky at Seville (Spain) from May 1982 to September 1984," Atmos. Environ. **21**, 1477–1481 (1987).
28. N. J. Pust, A. R. Dahlberg, M. J. Thomas, and J. A. Shaw, "Comparison of full-sky polarization and radiance observations to radiative transfer simulations which employ AERONET products," Opt. Express **19**, 18602–18613 (2011).
29. C. F. Bohren and E. E. Clothiaux, *Fundamentals of Atmospheric Radiation* (Wiley-VCH, 2006), pp. 349–354.
30. K. L. Coulson, *Polarization and Intensity of Light in the Atmosphere* (A. Deepak, 1988), p. 554.
31. C. F. Bohren and E. E. Clothiaux, *Fundamentals of Atmospheric Radiation* (Wiley-VCH, 2006), pp. 378–382. Here the authors show how linearly polarized light that illuminates particles that are large compared with the wavelength can be scattered as weakly circularly polarized light (i.e., circular polarization caused by multiple scattering).
32. Pika II hyperspectral imaging system from Resonon, Inc., Bozeman, Montana, USA (http://www.resonon.com). The system consists of a digital camera that has an internal diffraction grating and is coupled to a rotation stage controlled by a precision stepper motor and laptop computer. In this pushbroom system, the laptop acquires 640 different skylight spectra at each rotation stage position (i.e., for each line of the resulting hyperspectral datacube).
33. K. L. Coulson, *Polarization and Intensity of Light in the Atmosphere* (A. Deepak, 1988), p. 254.
34. C. F. Bohren and D. R. Huffman, *Absorption and Scattering of Light by Small Particles* (Wiley, 1983), p. 50.
35. PR-650 spectroradiometer from Photo Research, Inc., Chatsworth, California, USA.
36. K. L. Coulson, *Polarization and Intensity of Light in the Atmosphere* (A. Deepak, 1988), p. 582.
37. R. Gerharz, "Self polarization in refractive systems," Optik **43**, 471–485 (1975).
38. K. L. Coulson, *Polarization and Intensity of Light in the Atmosphere* (A. Deepak, 1988), p. 556. Coulson's term for self-polarization is "parasitic polarization".
39. R. S. Loe and M. J. Duggin, "Hyperspectral imaging polarimeter design and calibration," Proc. SPIE **4481**, 195–205 (2002).
40. By design, some nonimaging spectroradiometers depolarize light between the lens and the instrument's diffraction grating. For example, see PR-650 SpectraScan SpectraColorimeter Operating Manual, Software Version 1.10 (Photo Research, 1996), Section 3, p. 4.
41. G. Wyszecki and W. S. Stiles, *Color Science: Concepts and Methods, Quantitative Data and Formulae*, 2nd ed. (Wiley, 1982), pp. 133–140.
42. Similar techniques are used in R. J. Kubesh, "Computer display of chromaticity coordinates with the rainbow as an example," Am. J. Phys. **60**, 919–923 (1992).
43. Sun photometer data on $\tau_{\mathrm{aer},\lambda}$ for total aerosol extinction are acquired and archived by AERONET at http://aeronet.gsfc.nasa.gov. $\tau_{\mathrm{aer},\lambda}$ data in Table 2 are from the stations closest to USNA: Goddard Space Flight Center in Greenbelt, Maryland, and the Smithsonian Environmental Research Center in Edgewater, Maryland.
44. Throughout this paper, we concentrate on the *shapes* of $P_{L\lambda}$ spectra rather than on identifying specific spectral *features*. However, the Pika II system does consistently detect such features, including the narrow $P_{L\lambda}$ local maxima near 761 nm caused by molecular oxygen absorption.
45. Data from $\phi_{\mathrm{rel}} \sim 270°$ (Fig. 4) are compared with that from $\phi_{\mathrm{rel}} = 90°$ (Fig. 1) because both Ψ and compass azimuth ϕ are nearly equal in the two scenes. Having equivalent ϕ at a given h_0 reduces the $P_{L\lambda}$ effects of spatial changes in land and water spectral reflectances near our site.
46. C. Emde, R. Buras, B. Mayer, and M. Blumthaler, "The impact of aerosols on polarized sky radiance: model development, validation, and applications," Atmos. Chem. Phys. **10**, 383–396 (2010). MYSTIC is an acronym formed from "Monte Carlo code for the phYSically correct Tracing of photons In Cloudy atmospheres".

47. Aerosol concentrations and composition in the USNA region are analyzed in B. I. Magi, P. V. Hobbs, T. W. Kirchstetter, T. Novakov, D. A. Hegg, S. Gao, J. Redemann, and B. Schmid, "Aerosol properties and chemical apportionment of aerosol optical depth at locations off the U. S. east coast in July and August 2001," J. Atmos. Sci. **62**, 919–933 (2005).
48. N. J. Pust and J. A. Shaw, "Comparison of skylight polarization measurements and MODTRAN-P calculations," J. Appl. Remote Sens. **5**, 053529 (2011). MODTRAN is an acronym for "MODerate resolution atmospheric TRANsmission".
49. J. F. de Haan, P. B. Bosma, and J. W. Hovenier, "The adding method for multiple scattering calculations of polarized light," Astron. Astrophys. **183**, 371–391 (1987).
50. K. F. Evans and G. L. Stephens, "A new polarized atmospheric radiative transfer model," J. Quant. Spectrosc. Radiat. Transfer **46**, 413–423 (1991).
51. J. Lenoble, M. Herman, J. L. Deuzé, B. Lafrance, R. Santer, and D. Tanré, "A successive order of scattering code for solving the vector equation of transfer in the earth's atmosphere with aerosols," J. Quant. Spectrosc. Radiat. Transfer **107**, 479–507 (2007).
52. B. Mayer, "libRadtran: library for radiative transfer," http://www.libradtran.org.
53. M. Hess, P. Koepke, and I. Schult, "Optical properties of aerosols and clouds: The software package OPAC," Bull. Am. Meteorol. Soc. **79**, 831–844 (1998). OPAC is an acronym for "Optical Properties of Aerosols and Clouds".
54. $P_{L\lambda}$ for $h = 10°$ is included to allay any concerns that simulations for $h = 5°$ at any ϕ_{rel} might be corrupted by numerical instabilities arising from polRadTran's assumption of a plane-parallel atmosphere. In fact, the model's $P_{L\lambda}$ spectra change slowly and systematically for $h > 5°$.
55. J. V. Dave, "Extensive datasets of the diffuse radiation in realistic atmospheric models with aerosols and common absorbing gases," Sol. Energy **21**, 361–369 (1978).
56. L. S. Rothman, I. E. Gordon, A. Barbe, D. C. Benner, P. F. Bernath, M. Birk, V. Boudon, L. R. Brown, A. Campargue, J.-P. Champion, K. Chance, L. H. Coudert, V. Dana, V. M. Devi, S. Fally, J.-M. Flaud, R. R. Gamache, A. Goldman, D. Jacquemart, I. Kleiner, N. Lacome, W. J. Lafferty, J.-Y. Mandin, S. T. Massie, S. N. Mikhailenko, C. E. Miller, N. Moazzen-Ahmadi, O. V. Naumenko, A. V. Nikitin, J. Orphal, V. I. Perevalov, A. Perrin, A. Predoi-Cross, C. P. Rinsland, M. Rotger, M. Šimečková, M. A. H. Smith, K. Sung, S. A. Tashkun, J. Tennyson, R. A. Toth, A. C. Vandaele, and J. Vander Auwera, "The HITRAN 2008 molecular spectroscopic database," J. Quant. Spectrosc. Radiat. Transfer **110**, 533–572 (2009).
57. C. F. Bohren and E. E. Clothiaux, *Fundamentals of Atmospheric Radiation* (Wiley-VCH, 2006), pp. 378–379. Single-scattering calculations confirm that for small aerosols and typical mixtures of clean maritime aerosol species, the spectral dispersion of spherical scatterers' size parameters affects $P_{L\lambda}$ more than does dispersion of their collective n, k.
58. N. J. Pust and J. A. Shaw, "Wavelength dependence of the degree of polarization in cloud-free skies: simulations of real environments," Opt. Express **20**, 15559–15568 (2012).
59. J. S. Tyo, D. L. Goldstein, D. B. Chenault, and J. A. Shaw, "Review of passive imaging polarimetry for remote sensing applications," Appl. Opt. **45**, 5453–5469 (2006).